

## Evaluation of PBL Parameterizations in WRF at Subkilometer Grid Spacings: Turbulence Statistics in the Dry Convective Boundary Layer

HYEYUM HAILEY SHIN\* AND JIMY DUDHIA

*National Center for Atmospheric Research,<sup>+</sup> Boulder, Colorado*

(Manuscript received 29 May 2015, in final form 31 December 2015)

### ABSTRACT

Planetary boundary layer (PBL) parameterizations in mesoscale models have been developed for horizontal resolutions that cannot resolve any turbulence in the PBL, and evaluation of these parameterizations has been focused on profiles of mean and parameterized flux. Meanwhile, the recent increase in computing power has been allowing numerical weather prediction (NWP) at horizontal grid spacings finer than 1 km, at which kilometer-scale large eddies in the convective PBL are partly resolvable. This study evaluates the performance of convective PBL parameterizations in the Weather Research and Forecasting (WRF) Model at subkilometer grid spacings. The evaluation focuses on resolved turbulence statistics, considering expectations for improvement in the resolved fields by using the fine meshes. The parameterizations include four nonlocal schemes—Yonsei University (YSU), asymmetric convective model 2 (ACM2), eddy diffusivity mass flux (EDMF), and total energy mass flux (TEMF)—and one local scheme, the Mellor–Yamada–Nakanishi–Niino (MYNN) level-2.5 model.

Key findings are as follows: 1) None of the PBL schemes is scale-aware. Instead, each has its own best performing resolution in parameterizing subgrid-scale (SGS) vertical transport and resolving eddies, and the resolution appears to be different between heat and momentum. 2) All the selected schemes reproduce total vertical heat transport well, as resolved transport compensates differences of the parameterized SGS transport from the reference SGS transport. This interaction between the resolved and SGS parts is not found in momentum. 3) Those schemes that more accurately reproduce one feature (e.g., thermodynamic transport, momentum transport, energy spectrum, or probability density function of resolved vertical velocity) do not necessarily perform well for other aspects.

---

### 1. Introduction

Atmospheric mesoscale models with horizontal grid spacings of  $O(10\text{--}100)$  km have used one-dimensional planetary boundary layer (PBL) parameterizations to represent subgrid-scale (SGS) turbulence in the PBL. The conventional PBL parameterizations are designed on the assumption that all the turbulent motions in the PBL are SGS, as well as being horizontally homogeneous.

---

\* Current affiliation: NOAA/Geophysical Fluid Dynamics Laboratory, Princeton, New Jersey, and University Corporation for Atmospheric Research, Boulder, Colorado.

<sup>+</sup> The National Center for Atmospheric Research is sponsored by the National Science Foundation.

---

*Corresponding author address:* Hyeyum Hailey Shin, NOAA/Geophysical Fluid Dynamics Laboratory, Princeton University Forrestal Campus, 201 Forrestal Rd., Princeton, NJ 08540.  
E-mail: hyeyum.shin@noaa.gov

Meanwhile, running atmospheric mesoscale models at subkilometer horizontal grid spacing has become more practical in the past few years, with continuing advances in computing power. The smallest resolvable scale for a subkilometer grid spacing is comparable to the scale of large eddies in the convective boundary layer (CBL), and the conventional PBL parameterizations for the CBL do not perform properly with their assumptions at such a fine grid spacing. On the other hand, large-eddy simulation (LES) models have been used for explicitly simulating the large eddies in the CBL. The SGS turbulence parameterizations for the LES models assume homogeneous and isotropic SGS turbulence, and the LES models are consistent with their design when the smallest resolvable scale is in the inertial subrange. Since neither traditional PBL parameterizations nor LES SGS parameterizations perform appropriately at subkilometer grid sizes, the grid sizes fall within a “terra incognita” (Wyngaard 2004) in modeling the CBL. Mesoscale modeling communities also call this grid-size range the “gray zone.”

A number of previous studies attempted to parameterize the SGS turbulence and reproduce convective PBLs for subkilometer grid sizes, by using conventional PBL parameterizations and/or modifying them: [Honnert et al. \(2011, 2014\)](#) for a mass-flux parameterization, [Boutle et al. \(2014\)](#) and [Shin and Hong \(2015\)](#) for the  $K$ -profile models that originated from the Troen–Mahrt ([Troen and Mahrt 1986](#)) model, and [Ito et al. \(2015\)](#) for the Mellor–Yamada ([Mellor and Yamada 1982](#)) model. There are also a number of studies that extended the use of the LES SGS parameterizations to turbulence modeling in the gray zone ([Zhou et al. 2014](#); [Efstathiou and Beare 2015](#)). Each of the previous studies evaluated a certain type of the conventional parameterizations at gray-zone grid spacings and identified its errors in the gray zone, either suggesting ways to revise the parameterization or actually revising the parameterization for removing the errors.

In this study, five convective PBL parameterizations in the Weather Research and Forecasting (WRF) Model are evaluated at subkilometer grid spacings, with a focus on mean, resolved, and parameterized vertical fluxes, energy spectrum, and probability density functions (PDFs) of resolved vertical velocity. The five parameterizations are the Yonsei University (YSU; [Hong et al. 2006](#)), asymmetric convective model 2 (ACM2; [Pleim 2007a](#)), eddy diffusivity mass flux (EDMF; [Pergaud et al. 2009](#)), total energy mass flux (TEMF; [Angevine et al. 2010](#)), and Mellor–Yamada–Nakanishi–Niino (MYNN; [Nakanishi and Niino 2009](#)) schemes. Note that this study focuses on the parameterization of vertical transport. Horizontal transport is computed by an LES SGS parameterization, and our sensitivity experiments confirm that the parameterization of horizontal transport has little effect on the key findings of this study.

The main aim of this article is to document a priori how various types of PBL schemes behave on scales that permit resolved eddies. Our study is differentiated from the previous studies that evaluated the conventional PBL schemes in the gray zone, in that we compare the performance of various types of PBL schemes under the same experimental conditions. This study is also different from other intercomparison studies that compare the PBL parameterizations for grid sizes where the turbulent motions in the CBL are entirely SGS. The studies were limited to evaluating the parameterizations in terms of mean profiles and parameterized total turbulent transport profiles ([Pleim 2007b](#); [Li and Pu 2008](#); [Steenefeld et al. 2008](#); [Hu et al. 2010](#); [Shin and Hong 2011](#)). However,

for subkilometer grid sizes it is seen that some PBL schemes start to allow resolved-scale motions, and resolved turbulence statistics parameters should be evaluated, especially considering the expectations for the improvement in resolved fields by using fine meshes.

The paper is organized as follows. [Section 2](#) describes experimental setup: a brief description of the WRF model and the PBL parameterizations tested in this study. Evaluation results are presented in [section 3](#). [Section 4](#) provides summary and concluding remarks. The [appendix](#) describes details of the parameterization of horizontal transport.

## 2. Experimental setup

To evaluate the performance of PBL models at subkilometer grid sizes, a reference (REF) dataset in the grid-size range is made by filtering LES output. For this purpose, the LES run for an ideal CBL is conducted at horizontal grid spacing ( $\Delta_{\text{LES}}$ ) of 25 m and vertical grid spacing ( $\Delta_{z_{\text{LES}}}$ ) of 20 m, over the horizontal domain  $D^2 = 8^2 \text{ km}^2$  with the model top at  $z = 2 \text{ km}$ . Time step for the LES run ( $\Delta t_{\text{LES}}$ ) is 0.25 s. The CBL is forced by a constant surface heat flux and geostrophic wind [ $(\overline{w'\theta'_{\text{SFC}}}, U_g) = (0.20 \text{ K m s}^{-1}, 10.0 \text{ m s}^{-1})$ ]. Then, the LES results are spatially filtered for the filter sizes  $\Delta = 250, 500, \text{ and } 1000 \text{ m}$ . The filtered reference fields are considered as the “truth” on the subkilometer grid sizes.

This method has been one of the most popular ways of evaluating mesoscale models with gray-zone grid sizes because the reference data made in this way provide both resolved and subgrid-scale information (cf. [Cheng et al. 2010](#); [Honnert et al. 2011](#); [Dorrestijn et al. 2013](#); [Shin and Hong 2013](#); [Zhou et al. 2014](#); [Honnert et al. 2014](#); [Shin and Hong 2015](#)). For the details of the LES model setup and the reference data used in this study, refer to [Shin and Hong \(2015\)](#).

### a. Model setup

The ideal CBL is reproduced by the WRF Model ([Skamarock et al. 2008](#)) version 3.5.1. The surface momentum flux is calculated in a surface-layer scheme using Monin–Obukhov theory. The roughness length is 0.1 m and Coriolis parameter is set as  $f = 10^{-4} \text{ s}^{-1}$ . The initial wind profile is given by  $(u, v) = (10.0 \text{ m s}^{-1}, 0.0 \text{ m s}^{-1})$ , and the initial potential temperature is

$$\theta = \begin{cases} 300 \text{ K} & : 0 < z \leq 925 \text{ m} \\ 300 \text{ K} + (z - 925 \text{ m}) \times 0.0536 \text{ K m}^{-1} & : 925 < z \leq 1075 \text{ m} \\ 308.05 \text{ K} + (z - 1075 \text{ m}) \times 0.003 \text{ K m}^{-1} & : z > 1075 \text{ m} \end{cases} \quad (1)$$

TABLE 1. Summary of surface and bulk PBL parameters averaged for a time period of  $3t_0-4t_0$ : surface friction velocity  $u_*$ , convective velocity scale  $w_*$ , ratio of the two velocity scales ( $u_*/w_*$ ), PBL height  $z_i$ , and entrainment ratio  $A$  ( $A = \langle w'\theta' \rangle_{z_i} / \langle w'\theta' \rangle_{\text{SFC}}$ ). Errors from the reference, which are normalized by the reference values, are presented in percentage terms in the parentheses. Results for experiments with 500-m horizontal grid spacing and high vertical resolution ( $N_z = 100$ ) are presented.

	$u_*$ (m s <sup>-1</sup> )	$w_*$ (m s <sup>-1</sup> )	$u_*/w_*$	$z_i$ (m)	$A$
REF	0.51	1.89	0.26	1061.00	0.187
YSU	0.54 (5.8)	1.90 (0.5)	0.28 (7.6)	1069.12 (0.7)	0.188 (0.5)
ACM2	0.58 (13.7)	1.87 (1.0)	0.31 (19.2)	1020.42 (-3.8)	0.073 (-60.0)
EDMF	0.53 (3.9)	1.89 (0.0)	0.28 (7.6)	1047.63 (-1.2)	0.117 (-37.0)
TEMF	0.44 (-13.7)	1.90 (0.5)	0.23 (-10.7)	1076.17 (1.4)	0.159 (-14.9)
MYNN	0.54 (5.8)	1.89 (0.0)	0.28 (7.6)	1055.20 (-0.5)	0.149 (-20.3)

Small random perturbations of  $[-0.05 \text{ K}, 0.05 \text{ K}]$  are imposed on the initial temperature fields at the lowest four levels. Moisture is not included. We note that the surface heat flux is prescribed in this study, while NWP models use interactive land surface models for computing the flux. To investigate the robustness of the current results to the method of calculating surface heat flux, we conducted a set of sensitivity experiments that use surface layer schemes to compute the surface heat flux with a prescribed surface temperature. The temperature in the sensitivity experiments was tuned to have a similar domain-averaged surface heat flux with the previously prescribed flux ( $0.2 \text{ K m s}^{-1}$ ). The main difference from the original experiments is that the surface heat flux in the sensitivity experiments now has spatial variation, as the flux interacts with turbulent atmosphere. It was confirmed that key findings in this article, which are listed in abstract, remain unchanged in the sensitivity experiments (not shown).

The horizontal model domain size is  $8^2$ ,  $16^2$ , and  $32^2 \text{ km}^2$  for horizontal grid mesh ( $\Delta$ ) of 250, 500, and 1000 m, respectively. The number of horizontal grid points is  $32^2$ . The model top is located at  $z = 2 \text{ km}$ , and two vertical grid sizes are tested. One is a high resolution with  $\Delta z = 20 \text{ m}$  (i.e., the number of vertical grid points,  $N_z$ , is 100), which is comparable to the typical LES resolution for CBL simulations. The other is a low resolution,  $\Delta z = 100 \text{ m}$  (i.e.,  $N_z = 20$ ), typical of the mesoscale modeling resolution. The time step ( $\Delta t$ ) is 2.5, 5, and 10 s for  $\Delta$  of 250, 500, and 1000 m, respectively.

For the temporal discretization, the third-order Runge–Kutta time integration scheme is selected for low-frequency modes, and a time-split integration scheme is used for high-frequency modes. The fifth-order (third order) accurate finite-differencing advection scheme is used for horizontal (vertical) advection, with an Arakawa C grid system. SGS turbulence parameterization from Deardorff (1980), which is based on the three-dimensional turbulent kinetic energy (TKE), is selected for parameterizing horizontal transport (see the appendix). Vertical transport is conducted

by one-dimensional PBL parameterizations. Note that this study focuses on the parameterization of vertical transport, and our sensitivity experiments confirm that the parameterization of horizontal transport has little effect on the key findings of this study.

The one-dimensional PBL parameterizations include the YSU (Hong et al. 2006), ACM2 (Pleim 2007a), EDMF (Pergaud et al. 2009), TEMF (Angevine et al. 2010), and MYNN level 2.5 (Nakanishi and Niino 2009) models. Note that each PBL parameterization is tied to particular surface-layer schemes, which results in different surface friction velocities (and therefore surface momentum fluxes) among the five PBL parameterizations (cf. Table 1 and relevant information in section 3). The PBL parameterizations are described in the next subsection.

### b. A brief description of the PBL parameterizations

In this subsection, we describe only the CBL part of the PBL parameterizations and where  $z \leq z_i$  ( $z_i$  is the height of CBL) because the CBL is the focus of this paper. The PBL parameterizations calculate time tendencies of resolved variables  $\bar{c}^\Delta$  (the overbar with  $\Delta$  indicates the resolved part; i.e.,  $c = \bar{c}^\Delta + c'$ ) due to unresolved vertical transport ( $\overline{w'c'}$ ) [Eq. (2)], via the representation of the turbulent transport [Eq. (3)]:

$$\frac{\partial \bar{c}^\Delta}{\partial t} = \dots - \frac{\partial \overline{w'c'}}{\partial z}, \quad (2)$$

$$\overline{w'c'} = -K_c \frac{\partial \bar{c}^\Delta}{\partial z} + C_{\text{NL}}, \quad (3)$$

where  $K_c$  is the vertical diffusivity for the variable  $c$ , and  $C_{\text{NL}}$  is a nonlocal transport term for representing the transport against the local gradient  $\partial \bar{c}^\Delta / \partial z$ .

The YSU and ACM2 schemes are first-order schemes, and they represent  $K_c$  using the variables calculated from the first-order moments (i.e.,  $\bar{c}^\Delta$ ):

$$K_{u,v} = k w_s z \left(1 - \frac{z}{h}\right)^2 \quad \text{and} \quad K_{\theta,q} = \text{Pr}^{-1} K_{u,v}, \quad (4)$$

where  $k$  is the von Kármán constant ( $k = 0.4$ ),  $w_s$  is the velocity scale ( $w_s^3 = u_*^3 + bw_*^3$ ;  $u_*$  is the surface friction velocity,  $w_*$  is the convective velocity scale, and  $b$  is a proportional constant),  $h$  is the PBL height calculated by each PBL scheme, and  $Pr$  is the Prandtl number.

On the other hand, the EDMF, TEMF, and MYNN level 2.5 schemes are 1.5-order schemes (i.e., based on the TKE). The TKE [ $e = (u'^2 + v'^2 + w'^2)/2$ , a second-order moment] is needed to compute  $K_c$  in the TKE schemes:

$$K_c = l\sqrt{e}S_c, \quad (5)$$

where  $l$  is a mixing length,  $S_c$  is a stability function, and an additional prognostic equation is needed to calculate  $e$ . Each TKE scheme has its own way to calculate  $l$ ,  $e$ , and  $S_c$ . Note that the TEMF scheme uses a concept of total turbulent energy (TE), instead of TKE [i.e.,  $TE = TKE + \text{turbulent potential energy}$ , and TE replaces TKE in Eq. (5)]. In the statistically neutral and stable regions,  $TE = TKE$  (Angevine et al. 2010).

There is another way to classify PBL parameterizations (i.e., nonlocal and local parameterizations) according to the inclusion of the nonlocal term ( $C_{NL}$ ).<sup>1</sup> The YSU, ACM2, EDMF, and TEMF schemes are nonlocal schemes. The MYNN level 2.5 model is a local scheme ( $C_{NL} = 0$ ).

In the YSU scheme (Hong et al. 2006),

$$C_{NL} = K_c\gamma_c + \overline{w'c'_h} \left(\frac{z}{h}\right)^3, \quad (6)$$

where  $\gamma_c$  is a correction term to the local gradient, and  $\overline{w'c'_h}$  is an estimated flux at  $h$ . The second term on the right-hand side is an explicit inclusion of the entrainment flux, which is a unique feature of the scheme.

In the ACM2 (Pleim 2007a),

$$C_{NL} = M2u\bar{c}_1^\Delta - M2d_k\bar{c}_k^\Delta + M2d_{k+1}\bar{c}_{k+1}^\Delta \frac{\Delta z_{k+1}}{\Delta z_k}. \quad (7)$$

The subscript  $k$  indicates the  $k$ th vertical level;  $M2u$  is the height-independent upward convective mixing rate, and  $M2d_k$  is the height-dependent downward mixing rate from the layer  $k$  to the layer  $k - 1$ . The formulation represents the asymmetric mass flux in the CBL: the

rapid upward transport in convectively buoyant plumes [i.e., the first term on the right-hand side in Eq. (7)] and gradual downward transport due to compensatory subsidence [i.e., the second and third terms on the right-hand side in Eq. (7)].

The EDMF and TEMF are mass-flux schemes, and they parameterize nonlocal transport via an explicit representation of mass flux using updraft properties:

$$C_{NL} = M_u(c_u - \bar{c}^\Delta), \quad (8a)$$

$$M_u = a_u w_u. \quad (8b)$$

Here,  $M_u$  is the convective mass flux,  $a_u$  is the updraft fraction area,  $w_u$  is the vertical velocity in the updraft in CBL, and  $c_u$  is the updraft value of  $c$  (Pergaud et al. 2009). Updraft models are required to compute the updraft properties (i.e.,  $c_u$  and  $w_u$ ). For more information, refer to Pergaud et al. (2009) and Angevine et al. (2010).

It is worth noting that Honnert et al. (2011) revealed that the performance of conventional PBL parameterizations in the subkilometer and kilometeric grid-size range is largely determined by the inclusion of the nonlocal term. In this sense, comparing the five parameterizations characterized by different nonlocal terms could give guidance for a proper representation of the nonlocal transport term in mesoscale modeling in the gray zone.

### 3. Evaluation

The performance of the five CBL parameterizations is evaluated for the time period of  $3t_0$ – $4t_0$ , against the LES and filtered LES (i.e., the reference) data for the same time period, unless otherwise specified. Here,  $t_0 = 6\tau_*$  ( $\tau_*$  is the large-eddy turnover time), and it is the time required for the dynamic flow field of an LES run to reach a statistically quasi-equilibrium state (Moeng and Sullivan 1994). The value of  $t_0$  is roughly 3600 s for our CBL case. The time averaging keeps the sample size for turbulent statistics larger than 1000; without the time averaging, the sample size for the reference data at 1000-m grid spacing is only 64.

It is worth noting that the five PBL parameterizations are evaluated from  $3t_0$ , while our LES run is at equilibrium from  $t_0$  onward. This is because we aim to evaluate the performance of the PBL schemes after all 15 experiments (five PBL parameterizations for three grid sizes) reach their equilibrium. Figure 1 shows the evolution of the domain-averaged resolved TKE,  $\langle TKE \rangle^{R(\Delta)}$ , at  $0.5z_i$ . Values of  $\langle TKE \rangle^{R(\Delta)}$  for the YSU experiments at three grid sizes ( $\Delta$  of 250, 500, and 1000 m) are compared with the LES ( $\Delta_{LES} = 25$  m) and the reference at the three grid sizes. Note that  $\langle TKE \rangle^{R(\Delta)}$  for the LES

<sup>1</sup> In this study, a rather limited definition of nonlocal parameterization is adopted, which is generally used in mesoscale modeling communities. Note that in a broader sense, a parameterization is identified as a nonlocal parameterization when “the unknown quantity at one point in space is parameterized by values of known quantities at many points in space” (Stull 1988, p. 200); a nonlocal parameterization does not necessarily have  $C_{NL}$ .

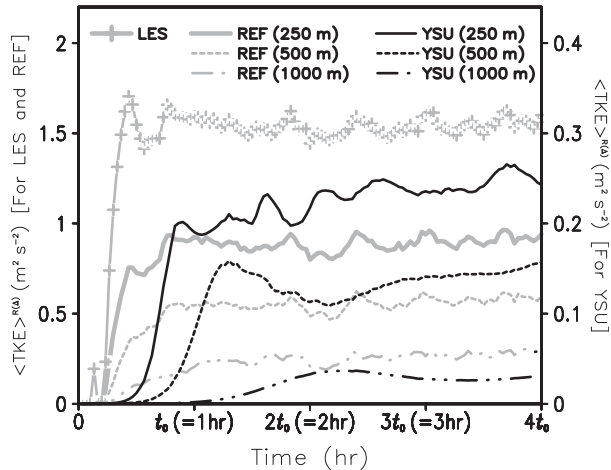


FIG. 1. Time evolution of the domain-averaged resolved turbulent kinetic energy  $\langle \text{TKE} \rangle^{R(\Delta)}$  at  $0.5z_i$ : LES with  $\Delta_{\text{LES}}$  of 25 m (solid gray with plus marks), reference (gray) and YSU experiment (black) with  $\Delta$  of 250 (solid), 500 (dotted), and 1000 m (dot-dot-dashed). The y-axis labeling on the left is for the LES and reference (REF), and the y-axis labeling on the right is for the YSU experiment.

increases in time until  $t = 1$  h and stops growing after that, supporting that the LES reaches a quasi-equilibrium state at about  $t = 1$  h (i.e.,  $t_0 = 1$  h). The reference  $\langle \text{TKE} \rangle^{R(\Delta)}$  values for the three grid sizes also reach the quasi-equilibrium state at the same time, since the reference data at each time step are obtained by spatially filtering the LES output.

On the other hand, the time required to reach a statistically quasi-equilibrium state is larger with coarser grid spacing for the experiments using the PBL schemes (cf. Ching et al. 2014; Zhou et al. 2014). The  $\langle \text{TKE} \rangle^{R(\Delta)}$  values for the YSU PBL scheme (black lines in Fig. 1) indicate that the time required for the YSU experiment to reach an equilibrium state is roughly  $t_0$  when  $\Delta = 250$  m,  $2t_0$  when  $\Delta = 500$  m, and  $3t_0$  when  $\Delta = 1000$  m.

Table 1 summarizes surface and bulk PBL parameters computed from the five PBL experiments and the reference: surface friction velocity  $u_*$ , convective velocity scale  $w_*$ , ratio of the two velocity scales ( $u_*/w_*$ ), PBL height  $z_i$ , and entrainment ratio  $A$  ( $A = \langle w'\theta' \rangle_{z_i} / \langle w'\theta' \rangle_{\text{SFC}}$ ). The angle brackets indicate a domain average. As the surface heat flux is prescribed, the errors in  $w_*$  do not exceed 1.0%. The errors in  $u_*$  are within  $\pm 13.7\%$ ;  $u_*$  is computed by different surface-layer schemes according to PBL schemes used (cf. section 2a), resulting in more divergent values than  $w_*$ . However, in the following subsections it will be shown that impacts of the difference in the surface drag are limited to the domain-averaged horizontal momentum transport and the momentum profiles. The

shear-buoyancy ratio ( $u_*/w_*$ ) can be used as an indicator of the onset of organized convective roll formulation (Sykes and Henn 1989; Moeng and Sullivan 1994). The  $u_*/w_*$  values of the LES and five PBL experiments range from 0.23 to 0.31, and these values are not in the convective roll regime.

a. Mean and total vertical transport profiles

Figure 2 presents the vertical profiles of horizontally domain-averaged potential temperature (i.e.,  $\langle \theta \rangle$ ) at  $3t_0$  and total (resolved plus parameterized) vertical heat flux (i.e.,  $\langle w'\theta' \rangle$ ) averaged for  $3t_0-4t_0$ , for the YSU, ACM2, EDMF, TEMF, and MYNN experiments in comparison with the LES profiles. Hereafter, angle brackets indicate a domain average. To normalize the height coordinate for the profiles (Figs. 2–4 and 7), a time-averaged LES PBL height (i.e., averaged for  $3t_0-4t_0$ ) is used (cf. Table 1). Figure 2 indicates that the horizontal grid size hardly affects the mean temperature and total heat flux profiles, so we focus on the differences due to the choice of PBL scheme and vertical resolution.

All the experiments reproduce the mixed-layer temperature well regardless of the vertical resolution, except for the TEMF experiment when  $N_z = 20$  (cf. Figs. 2d and 2i). For the high vertical resolution case ( $N_z = 100$ ), the temperature and flux profiles for the TEMF (Figs. 2d,i) and MYNN (Figs. 2e,j) experiments are almost identical to the LES profiles, while the other three experiments overestimate the temperature gradient in the entrainment zone (Figs. 2a–c). It is worth noting that the MYNN PBL scheme, a local scheme, also produces a weakly stable or neutral profile in the upper mixed layer, whereas previous studies have shown that local PBL schemes fail in reproducing that stability in their numerical weather prediction and/or general circulation models with model grid sizes of  $O(10-100$  km) (e.g., Holtslag and Boville 1993; Hong and Pan 1996). Note that our MYNN results are consistent with the findings of LeMone et al. (2013). They found that at 1-km grid spacing and with 25-point horizontal averaging, three local PBL schemes in the WRF model version 3.2—the Mellor–Yamada–Janjic (MYJ), quasi-normal scale elimination (QNSE), and Bougeault–LaCarrere (BouLac)—produce a slightly stable upper PBL, while the modeled upper PBL is unstable at 9-km and 27-km grid sizes. At these grid sizes, where none of turbulent eddies in the PBL are resolvable, local schemes have to maintain an unstable profile in order to produce vertical transport via the local diffusion formula (i.e.,  $\overline{w'\theta'} = -K_c \partial \bar{c}^\Delta / \partial z$ ) (Holtslag and Boville 1993). On the other hand, resolved motions produce significant transport at subkilometer grid sizes (cf. Fig. 4j), and the local

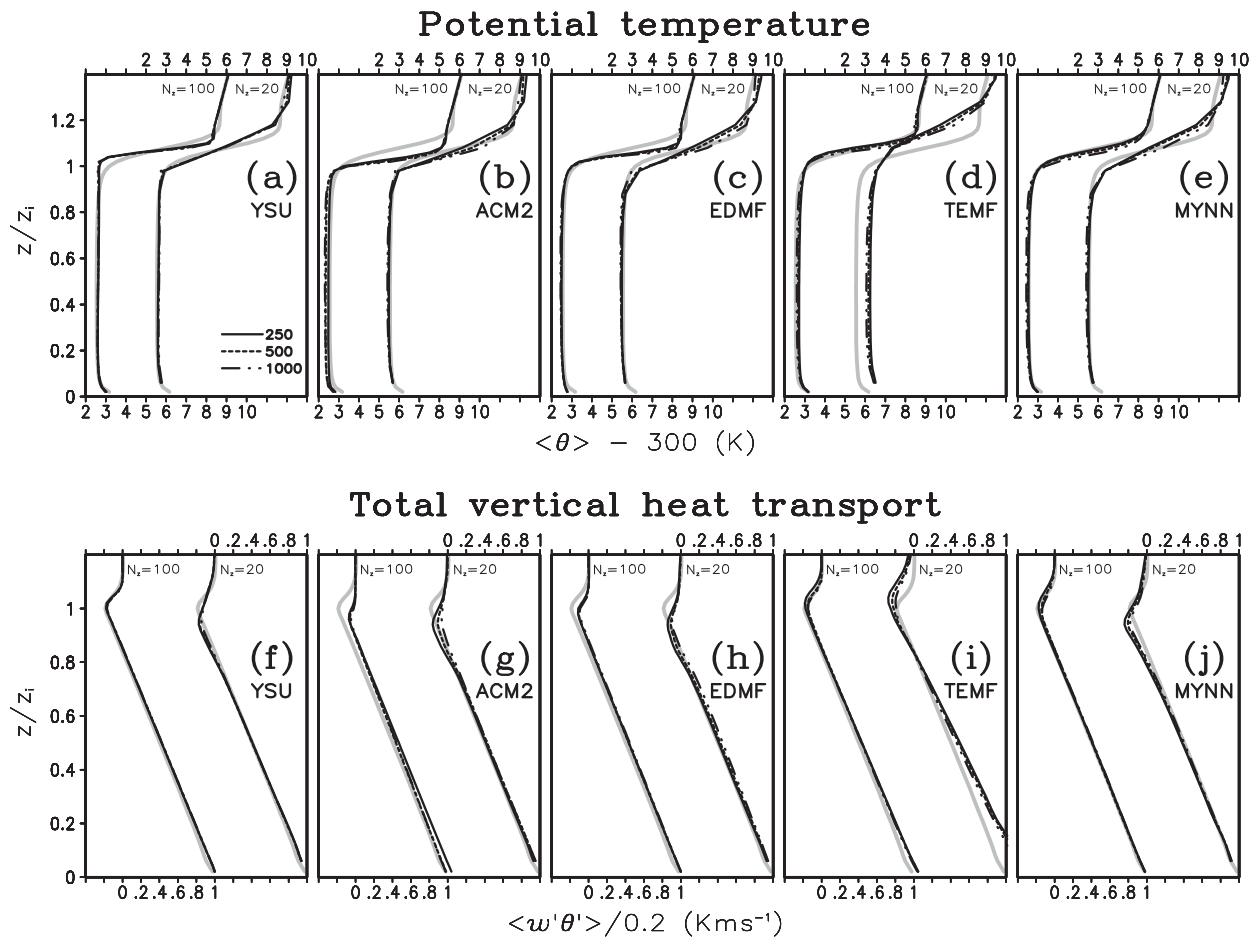


FIG. 2. Vertical profiles of domain-averaged (top) potential temperature  $\langle \theta \rangle$  and (bottom) total (total = resolved + parameterized) vertical heat flux  $\langle w'\theta' \rangle$  for (a),(f) YSU, (b),(g) ACM2, (c),(h) EDMF, (d),(i) TEMF, and (e),(j) MYNN experiments:  $\Delta = 250$  (solid), 500 (dotted), and 1000 m (dot–dot–dashed). The black and gray lines indicate results for experiments and LES, respectively. The bottom and top  $x$  axes in each panel are for  $N_z = 100$  and  $N_z = 20$ , respectively.

MYNN scheme does not need to maintain the unstable profile. Other local schemes in the current version of the WRF model—the MYJ scheme (Janjic 1994) and the University of Washington (UW) scheme (Bretherton and Park 2009)—also produce the stable or neutral profile (not shown). This supports the necessity of reevaluating existing PBL schemes at gray-zone grid spacings.

Unlike in the mixed layer, different PBL schemes show divergent results in the entrainment layer. Furthermore, when the vertical resolution used is too low to resolve an entrainment layer (i.e.,  $N_z = 20$ ), all the experiments overestimate the entrainment-layer depth. The effect of the vertical resolution is consistent with the findings of the previous studies, namely those of Sullivan and Patton (2011) and Efstathiou and Beare (2015). Sullivan and Patton (2011) showed that insufficient vertical resolution in the entrainment layer weakens the inversion and increases the entrainment rate, in their large-eddy simulations for a CBL case. Efstathiou

and Beare (2015) also found the increase in the entrainment rate in their numerical modeling at sub-kilometer grid spacings for CBLs. Note that in this study a vertical grid system with constant vertical resolution is used, which is frequently adopted in LES models and cloud-resolving models, while most NWP models adopt a vertical grid system with stretched vertical grid spacing. A set of model runs was conducted with the stretched vertical grid spacing and confirmed that the key results in the constant grid system are also found in the stretched grid system, while there are several changes in detail that are worthwhile mentioning. The modeled entrainment layer is deeper and the inversion is weaker when the stretched grid system is used, since vertical grid spacing in the entrainment layer is coarser in the stretched system. Among the five PBL schemes, the EDMF experiments lose much of resolved scale structures when the entrainment layer is less resolved by using the stretched grid system.

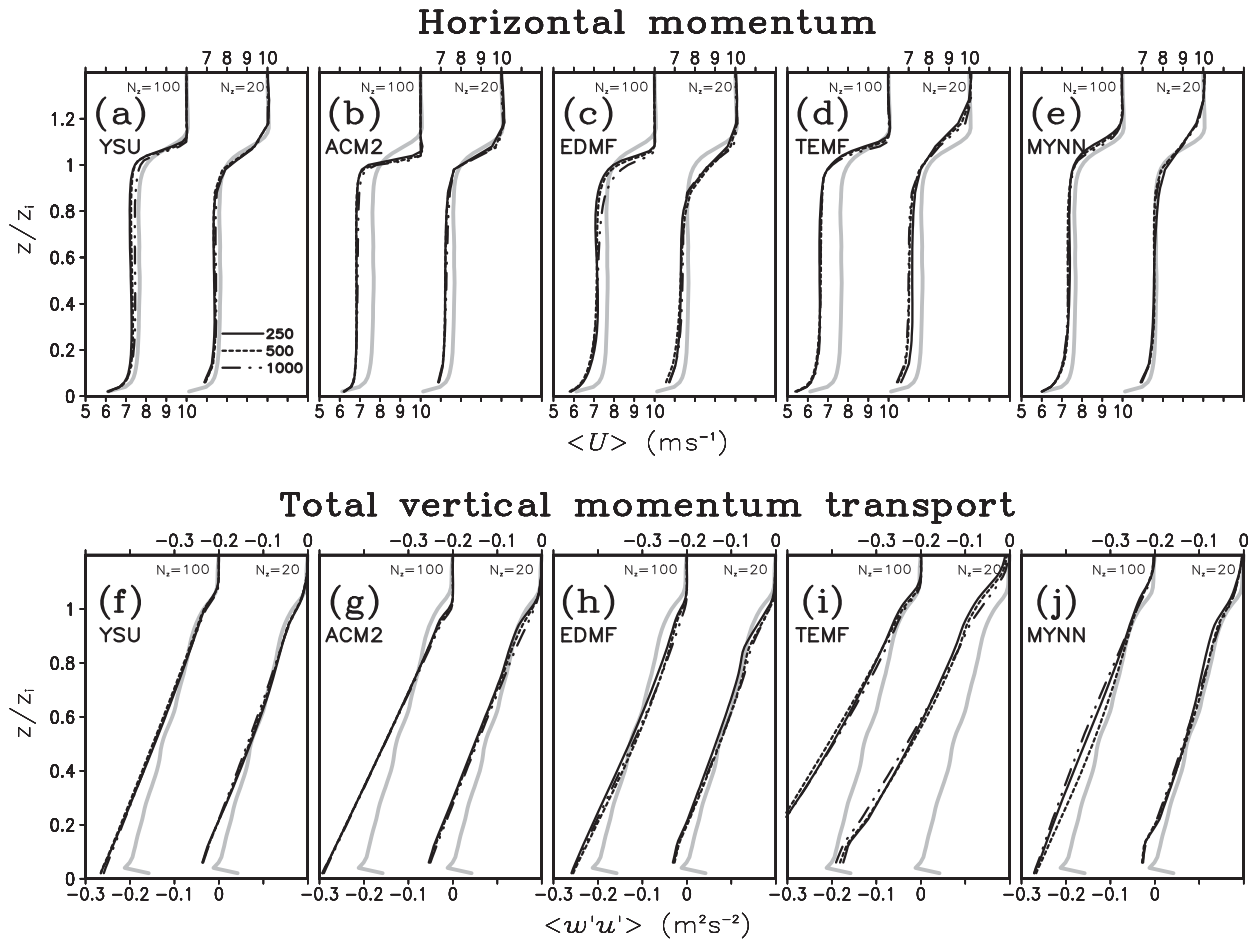


FIG. 3. As in Fig. 2, but for vertical profiles of domain-averaged (top) momentum  $\langle U \rangle$  and (bottom) total (total = resolved + parameterized) vertical momentum flux  $\langle w'u' \rangle$ .

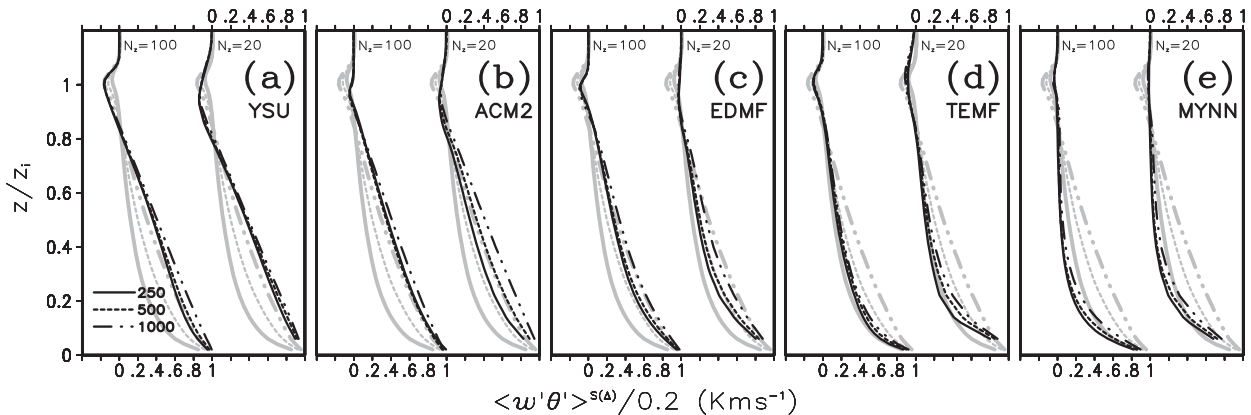
The vertical profiles of domain-averaged momentum (i.e.,  $\langle U \rangle$ ) at  $3t_0$  and total vertical momentum flux (i.e.,  $\langle w'u' \rangle$ ) for  $3t_0-4t_0$  are shown in Fig. 3. For the high vertical resolution case ( $N_z = 100$ ), all the experiments underestimate the mixed-layer momentum (Figs. 3a–e), owing to the overestimated surface drag (Figs. 3f–j). Note that Shin and Hong (2011) revealed that the amount of surface drag calculated by the surface-layer scheme determines modeled mixed-layer mean wind speed, while differences due to vertical transport algorithm (i.e., the PBL scheme) mainly appear near the top of the CBL (cf. their Fig. 10). The momentum profiles for the YSU and MYNN experiments are the most similar to the LES profile (Figs. 3a,e), followed by the EDMF experiment (Figs. 3c). In the ACM2 and TEMF experiments the values of the surface drag are over 1.5 times larger than the LES value (Figs. 3g,i), and then the mean momentum values are largely underestimated (Figs. 3b,d).

The comparison between the high and low vertical resolution cases indicates that the computed surface

drag is smaller in the low-resolution case for all PBL schemes. As a result, the wind profile is closer to the LES profile. Note that the lowest model level height ( $z_1$ ) is higher in the low-resolution case ( $z_1 \approx 50$  m) than that in the high-resolution case ( $z_1 \approx 10$  m). Shin et al. (2012) showed that the higher the  $z_1$  is, the smaller the calculated surface drag is; our results are consistent with their finding (Figs. 3f–j). In this case, the lower vertical resolution alleviates the high-drag bias mentioned above.

In summary, the mixed-layer mean temperature profiles modeled using the subkilometer grid sizes are less dependent on the choice of PBL parameterization and horizontal grid spacing, compared to those modeled using larger grid spacings (cf. Li and Pu 2008; Steeneveld et al. 2008; Hu et al. 2010; Shin and Hong 2011). On the other hand, the modeled mean momentum in the mixed layer and the mean temperature and momentum in the entrainment layer significantly depend on the choice of PBL scheme and vertical resolution.

## Subgrid-scale vertical heat transport



## Resolved vertical heat transport

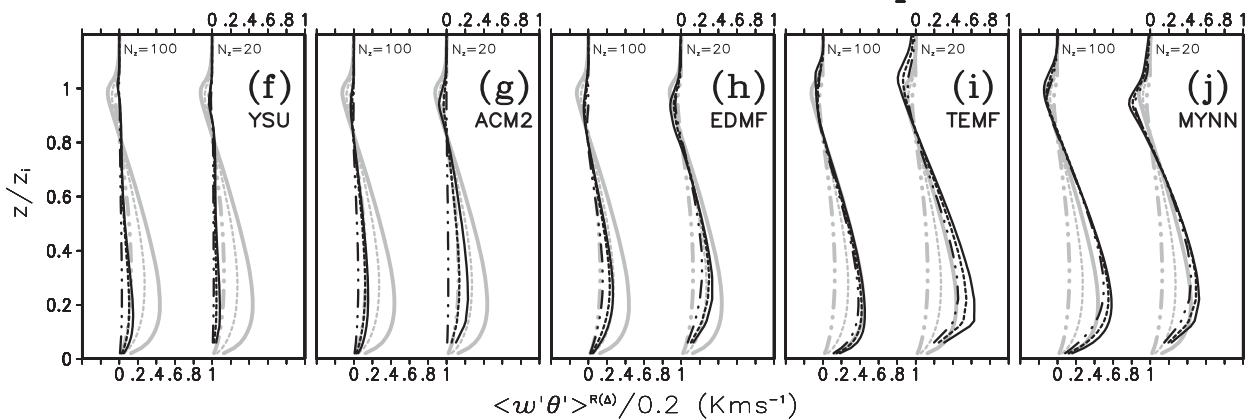


FIG. 4. As in Fig. 2, but for vertical profiles of domain-averaged (top) parameterized subgrid-scale (SGS) vertical heat transport and (bottom) resolved vertical heat transport.

### b. Parameterized and resolved vertical transport profiles

Figure 4 presents separation of the total heat flux into parameterized SGS part (Figs. 4a–e) and resolved part (Figs. 4f–j). Modeled results are compared with the reference for each grid size. The parameterized heat flux profiles for the different PBL schemes reveal that each PBL scheme has its own best-performing resolution (Figs. 4a–e). The YSU and ACM2 PBL schemes parameterize the SGS heat transport very closely to the reference transport profile for  $\Delta$  of 1000 m (Figs. 4a,b), regardless of actual grid size used. The SGS heat transport profiles computed by the EDMF are between the reference profiles for  $\Delta$  of 500 m and  $\Delta$  of 1000 m (Fig. 4c), while the TEMF and MYNN schemes parameterize the SGS transport like the reference for  $\Delta$  of 250 m (Figs. 4d,e) for the grid sizes tested.

The difference of each scheme from the reference in the parameterized heat transport (Figs. 4a–e) is

compensated by corresponding resolved transport (Figs. 4f–j). For example, the resolved heat transport in the YSU and ACM2 experiments is less than 25% of the total heat transport regardless of the horizontal grid spacing (Figs. 4f,g); the parameterized heat transport in these two experiments is more than 75% of the total transport for the all three grid sizes (cf. Figs. 4a,b). On the other hand, the resolved transport in the TEMF and MYNN experiments, which show the smaller amounts of the parameterized transport than the other three experiments (cf. Figs. 4d,e), is more than 60% and 80% of the total transport, respectively (Figs. 4i,j). This compensation is attributed to the fact that resolved  $\theta$  and  $w$  perturbations are strongly coupled, as the parameterized vertical heat transport directly affects not only  $\theta$ , but also  $w$  via buoyancy. Therefore, when SGS heat transport is overestimated, both resolved  $\theta$  and  $w$  perturbations are underestimated (not shown), leading to an underestimation in resolved heat transport. This compensation between the SGS heat transport and



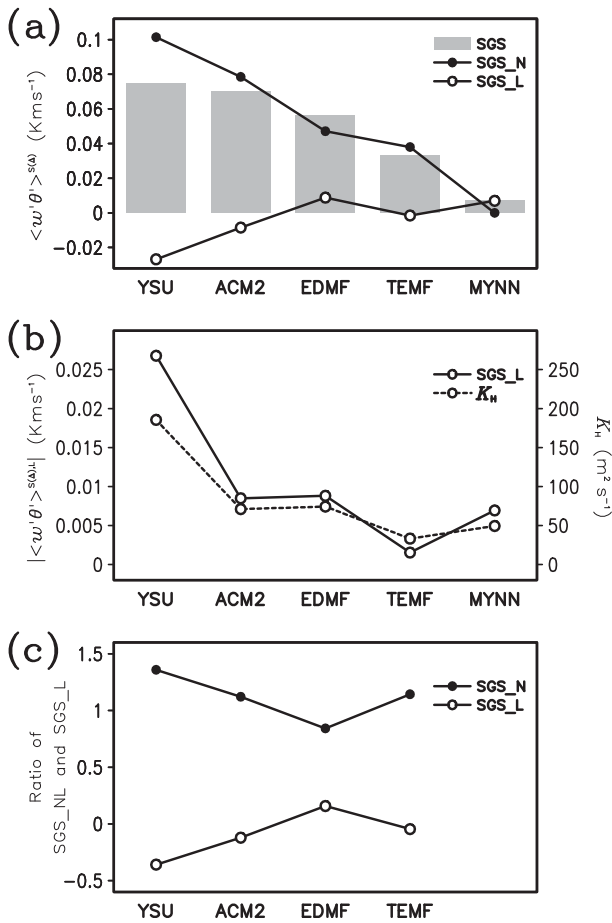


FIG. 5. (a) Parameterized total SGS (SGS nonlocal + SGS local) heat transport (SGS: gray bars), SGS nonlocal heat transport (SGS\_N: solid black with closed circles), and SGS local heat transport (SGS\_L: solid black with open circles) for YSU, ACM2, EDMF, TEMF, and MYNN experiments. (b) Absolute amount of the SGS local heat transport (solid black with open circles) and vertical diffusivity for heat ( $K_H$ : dotted black with open circles). (c) Ratio of the SGS nonlocal (solid black with closed circles) and SGS local (solid black with open circles) terms to total SGS transport, for four nonlocal PBL schemes: YSU, ACM2, EDMF, and TEMF. Results are shown for 500-m grid spacing, at  $z = 0.5z_i$ .

the resolved heat transport results in similar total transport profiles among the different experiments (cf. Figs. 2f–j), which are comparable to the LES profile, except for the entrainment zone. The compensation also explains why the temperature and total heat transport profiles are well reproduced regardless of PBL parameterization and horizontal resolution (cf. Fig. 2). There is also an exception, the TEMF experiment with  $N_z = 20$ ; the resolved transport is larger than it needs to be for the compensation (Figs. 4d,i). Therefore, the total heat transport is overestimated compared to the reference (Fig. 2i), leading to the warmer mixed layer than the

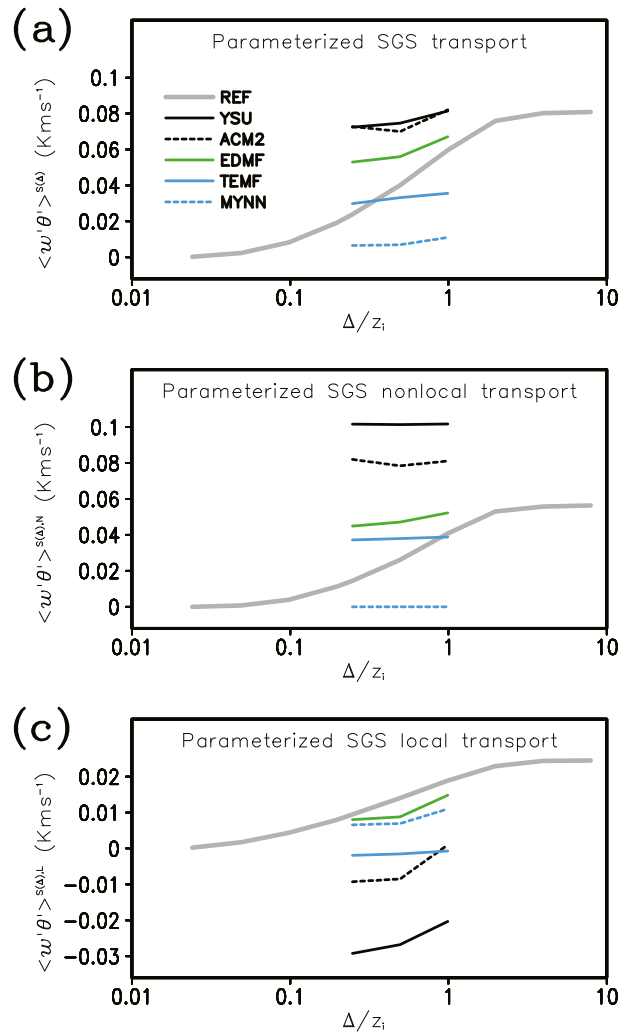


FIG. 6. Grid-size dependency of (a) total SGS heat transport, (b) SGS nonlocal heat transport, and (c) SGS local heat transport for the YSU (solid black), ACM2 (dotted black), EDMF (solid green), TEMF (solid blue), and MYNN (dotted blue) experiments, with corresponding reference (gray). Results at  $z = 0.5z_i$  are shown.

reference (Fig. 2d). This error can be mitigated by using a thin surface layer.

To investigate the underlying causes of the differences among the five schemes, we further analyze the nonlocal and local transport terms in the schemes (cf. section 2b): Figs. 5 and 6 and Table 2. Results are presented for the 500-m grid size, at  $z = 0.5z_i$ . For reference, the SGS nonlocal transport is defined as the vertical transport via strong updrafts of organized structures (e.g., thermals, rolls, and cells). The reference nonlocal transport is calculated by conditionally sampling strong-updraft LES grid points; then, vertical transport by the updraft points is computed. The local transport is defined as

TABLE 2. Differences in parameterized heat transport between 250-m and 1000-m experiments [i.e.,  $\langle w'\theta' \rangle^{S(1000\text{m})} - \langle w'\theta' \rangle^{S(250\text{m})}$ ] at  $0.5z_i$  are presented for five PBL schemes with corresponding reference differences: for total SGS heat transport, SGS nonlocal heat transport, and SGS local heat transport. In the parentheses, the differences normalized by the reference differences are presented.

	Total SGS heat transport ( $\text{K m s}^{-1}$ )	SGS nonlocal heat transport ( $\text{K m s}^{-1}$ )	SGS local heat transport ( $\text{K m s}^{-1}$ )
REF	0.035	0.026	0.009
YSU	0.009 (0.25)	0.000 (0.00)	0.009 (1.00)
ACM2	0.009 (0.25)	-0.001 (-0.03)	0.010 (1.11)
EDMF	0.014 (0.40)	0.007 (0.26)	0.007 (0.77)
TEMF	0.005 (0.14)	0.001 (0.03)	0.004 (0.44)
MYNN	0.004 (0.11)	0.00 (0.00)	0.004 (0.44)

the vertical transport via remaining small-scale turbulences. For more details, refer to [Shin and Hong \(2013\)](#) and [Shin and Hong \(2015\)](#).

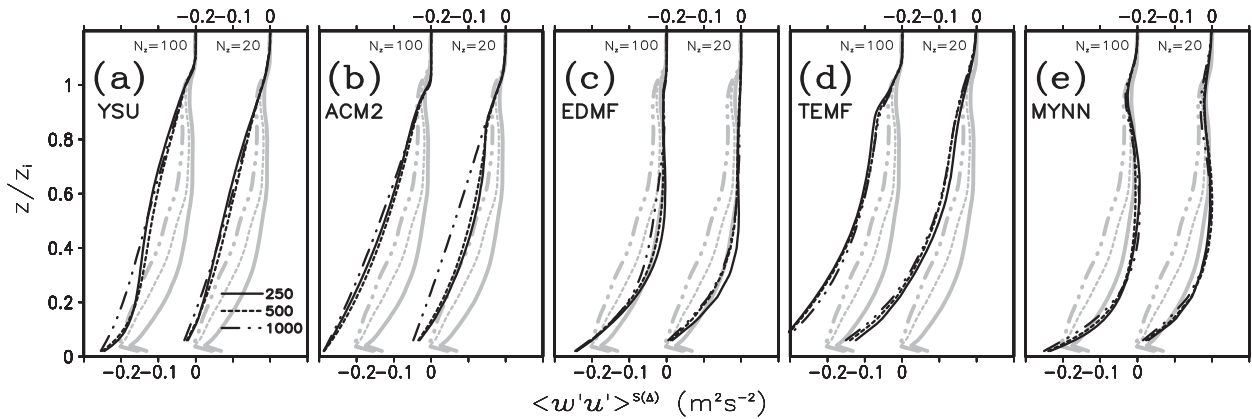
[Figure 5a](#) indicates a trend between the total SGS heat transport (cf. total SGS = SGS nonlocal + SGS local) and SGS nonlocal heat transport. The PBL parameterizations that calculate stronger total SGS heat transport have stronger SGS nonlocal transport (cf. gray bars and black line with closed circles in [Fig. 5a](#)). The local SGS heat transport tends to show the similar trend in terms of its magnitude ([Fig. 5b](#)), but it is not as obvious as the trend of the nonlocal heat transport. For example, the TEMF has the smallest value of the SGS local transport (in terms of its magnitude), whereas the MYNN has the smallest value of the total SGS transport. Note that the local transport terms in the YSU and ACM2 have negative values ([Fig. 5a](#)); the large nonlocal transport terms in the two schemes ([Fig. 5a](#)) stabilize the mixed layer, leading to the positive mean temperature gradients at the level (cf. [Figs. 2a and 2b](#)). The different amounts of the local heat transport among the five PBL schemes are mainly attributed to the different sizes of the vertical heat diffusivity ([Fig. 5b](#)) and the vertical mean gradients. Given that the contribution of the SGS nonlocal transport to the total SGS transport is more than 50% for the five PBL schemes ([Fig. 5c](#)), the differences in the parameterized heat transport among the five PBL schemes shown in [Figs. 4a–e](#) are mainly attributed to the differences in the nonlocal transport. These findings are kept regardless of model grid spacing (not shown). Our results are consistent with the finding of [Honnert et al. \(2011\)](#). They showed that for the turbulence parameterization in the MesoNH mesoscale model, the activation of the mass-flux term in the parameterization has the most significant effect on its performance at subkilometer and kilometeric grid sizes, among the following three factors: mixing in three dimensions or mixing in vertical, mixing length used in calculating the vertical diffusivity, and activation of the mass-flux term.

[Figure 6](#) compares horizontal grid-size dependency of the total SGS heat transport, SGS nonlocal transport,

and SGS local transport. As indicated by [Fig. 4](#), none of the tested PBL schemes is as scale-aware as the reference is ([Fig. 6a](#)). [Table 2](#) shows that the difference in the parameterized heat transport between the experiments for 250-m grid size and 1000-m grid size for each scheme is less than or equal to 25% of the reference difference, except for the EDMF scheme. The EDMF scheme has the largest resolution dependency among the five PBL schemes, but even the largest dependency is 40% of the reference dependency. [Figure 6b](#) and [Table 2](#) indicate that the small resolution dependency for each PBL scheme is mainly attributed to the nonlocal transport, which is hardly dependent on the horizontal grid size; even the grid-size dependency for the EDMF scheme is only 26% of the reference grid-size dependency ([Table 2](#)). Several recent studies introduced modifications of nonlocal transport terms in convective PBL parameterizations to effectively reduce the nonlocal transport for increasing model resolution, aiming at making the parameterizations work at gray-zone resolutions ([Honnert et al. 2014](#); [Shin and Hong 2015](#)). [Honnert et al. \(2014\)](#) modified the mass-flux term in the EDMF parameterization and [Shin and Hong \(2015\)](#) replaced the gamma term in the YSU PBL scheme with an LES-based nonlocal flux profile. The parameterized local transport values for the YSU, ACM2, and EDMF experiments show large grid-size dependency, as large as 75% of the reference ([Fig. 6c](#) and [Table 2](#)). However, the total SGS transport terms for the three experiments are less dependent on the model grid spacing compared to the SGS local transport terms, since the nonlocal transport terms are larger than the local terms and their dependency on the model grid size is small (cf. [Figs. 5c](#) and [6b](#)).

[Figure 7](#) presents separation of the total momentum transport into parameterized SGS part ([Figs. 7a–e](#)) and resolved part ([Figs. 7f–j](#)). The momentum transport profiles show different features from the heat transport profiles. First of all, for each scheme, the best-performing resolution for the momentum transport and the resolution for the heat transport are not always the same. The parameterized momentum transport profiles for the YSU and ACM2 experiments are more negative than

### Subgrid-scale vertical momentum transport



### Resolved vertical momentum transport

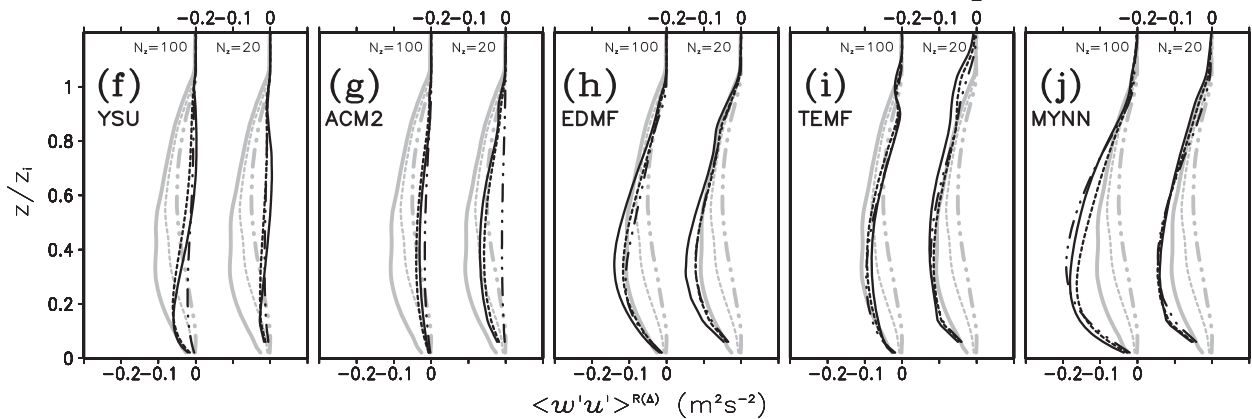


FIG. 7. Vertical profiles of domain-averaged (top) parameterized subgrid-scale (SGS) vertical momentum transport and (bottom) resolved vertical momentum transport, for (a),(f) YSU, (b),(g) ACM2, (c),(h) EDMF, (d),(i) TEMF, and (e),(j) MYNN experiments (black) with corresponding reference (gray):  $\Delta = 250$  (solid), 500 (dotted), and 1000 m (dot-dot-dashed). The bottom and top  $x$  axes in each panel are for  $N_z = 100$  and  $N_z = 20$ , respectively.

the reference SGS transport for  $\Delta$  of 1000 m (Figs. 7a,b), whereas for the SGS heat transport 1000-m grid size is the best performing grid size of the two schemes. The best-performing grid spacing of the EDMF scheme is 250 m for the momentum transport (Fig. 7c), while it is between 500 and 1000 m for the heat transport (Fig. 4c). The TEMF scheme calculates the largest SGS momentum transport among the five schemes (Fig. 7d), which is opposite to the heat transport. Only the MYNN scheme shows a consistent best-performing resolution between the momentum and heat (cf. Figs. 4e and 7e). Second, resolved momentum transport does not compensate for the deviation of parameterized momentum transport from the reference (Figs. 7f–j). Therefore, total momentum transport and mean momentum profiles are significantly affected by PBL parameterization (cf. Fig. 3). This is because  $u$  is loosely coupled with  $w$ , while  $\theta$  is directly coupled with  $w$  via buoyancy. Thus, an

overestimation of the SGS momentum transport results in an underestimation of  $u$  perturbation (not shown), while it does not guarantee an underestimation of  $w$  perturbation; the magnitude of  $w$  perturbation is more dependent on the parameterized heat transport. Therefore, the overestimation of the SGS momentum transport does not always result in an underestimation of resolved momentum transport, and there is no guarantee of compensation between the resolved and parameterized parts.

#### c. Resolved energy spectrum

PBL parameterizations directly affect resolved energy, via the dissipation of resolved motions. In other words, resolved convection is more energetic than it should be when relevant SGS transport is underestimated (Zhou et al. 2014), while overestimated SGS transport suppresses resolved motions, leading resolved convection to appear less energetic (LeMone et al. 2013;

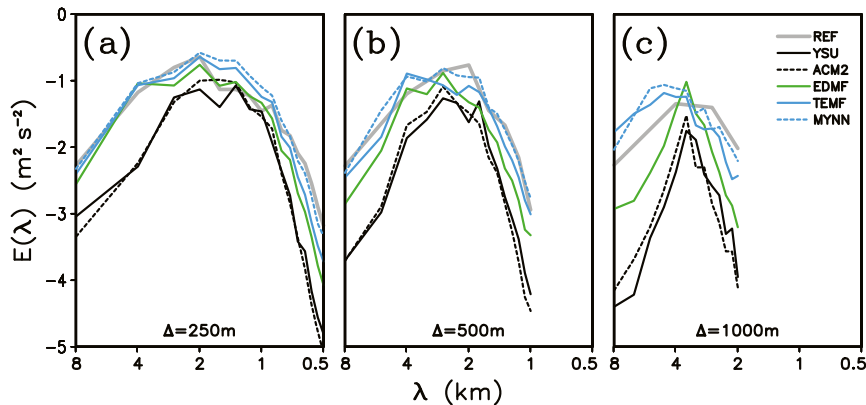


FIG. 8. Vertical velocity ( $w$ ) spectra at  $0.5z_i$  for YSU (solid black), ACM2 (dotted black), EDMF (solid green), TEMF (solid blue), and MYNN (dotted blue) experiments, with corresponding reference (solid gray):  $\Delta =$  (a) 250, (b) 500, and (c) 1000 m. Results for  $N_z = 100$  are shown. Note that both the  $x$  axis and  $y$  axis are scaled logarithmically.

Ching et al. 2014). Figure 8 presents two-dimensional spectra of resolved vertical velocity ( $w$ ) at  $0.5z_i$  for the reference and five PBL schemes. To compute each two-dimensional spectrum, the spectral coefficients for each experiment are calculated as a function of wavenumber vector  $\kappa_H = (\kappa_x, \kappa_y)$  by the discrete two-dimensional Fourier transform in the horizontal plane at  $z = 0.5z_i$ . Then, the coefficients are averaged in circular rings at constant  $|\kappa_H| = (\kappa_x^2 + \kappa_y^2)^{1/2}$  over time (cf. Sullivan and Patton 2011; Wyngaard 2010). Note that the experiments with the PBL schemes are affected by an implicit sixth-order numerical diffusion, owing to the fifth-order horizontal advection scheme used (Skamarock 2004). For a better evaluation the reference  $w$  fields are filtered by a sixth-order numerical filter, before computing the spectrum.

Figure 8 indicates a trend between the energy spectrum and the parameterized vertical heat transport. The YSU and ACM2 PBL schemes underestimate the resolved energy for all resolutions used (Fig. 8), consistent with the overestimation of the SGS heat transport (cf. Figs. 4a and 4b). The resolved energy is the largest in the TEMF and MYNN experiments among the five experiments for each grid size, as the resolved heat flux is (cf. Figs. 4i and 4j). This is because  $w$  is directly coupled with vertical heat transport via buoyancy, as mentioned in section 3b. The energy spectra from the weak-diffusion schemes (i.e., the TEMF and MYNN) are the closest to the reference spectra, compared to those from the YSU, ACM2, and EDMF schemes, except for the excessive energy at large scales ( $\lambda > 4$  km) when  $\Delta = 1000$  m.

#### d. Probability density function of resolved vertical velocity

To evaluate the PBL schemes in statistically representing turbulence structures in the PBL, a probability

density function is calculated for vertical velocity ( $w$ ). Figure 9 presents the PDFs of  $w$  at  $0.5z_i$ , based on the distributions of  $w$ . The area underneath each line is equal to 1. The PDF for LES ( $\Delta_{LES} = 25$  m) is positively skewed (Fig. 9a), indicating a few strong thermal updrafts surrounded by a large number (or area) of weak interthermal downdrafts (cf. Moeng and Sullivan 1994; Zhou et al. 2014). The reference fields for the sub-kilometer grid sizes also show a positive skewness (cf. Fig. 9b for 250-m  $\Delta$ , and Fig. 9c for 500-m  $\Delta$ ). The reference skewness (gray lines in Fig. 9) decreases as the filter size increases from 250 to 1000 m (Figs. 9b–d), and it approaches a nearly symmetric distribution at 1000-m  $\Delta$  (Fig. 9d) as shown previously by Huang et al. (2009) and Zhou et al. (2014).

When  $\Delta = 250$  m and  $\Delta = 500$  m (Figs. 9b,c), the modeled  $w$  fields are also positively skewed in all five experiments, while most schemes have defects in detail. The PDFs for the YSU and ACM2 experiments deviate the most from the reference among the five experiments; the number of grid points where  $|w| \geq 1$  m s<sup>-1</sup> (i.e., the number of grid points where vertical motions are strong) is much less than that for the reference, while there are many more grid points where vertical motions are weak (i.e., the grid points where  $|w| < 1$  m s<sup>-1</sup>). The other three experiments, especially the EDMF experiment for 500-m grid spacing, follow the reference PDF well. For  $\Delta$  of 1000 m (Fig. 6d), only the EDMF experiment shows a nearly symmetric distribution as in the reference. These features shown in the high vertical resolution experiments ( $N_z = 100$ ) are kept in the low vertical resolution experiments ( $N_z = 20$ ) (not shown).

The energy spectrum analysis and PDF analysis indicate that those schemes that more accurately reproduce the PDF do not necessarily perform well for

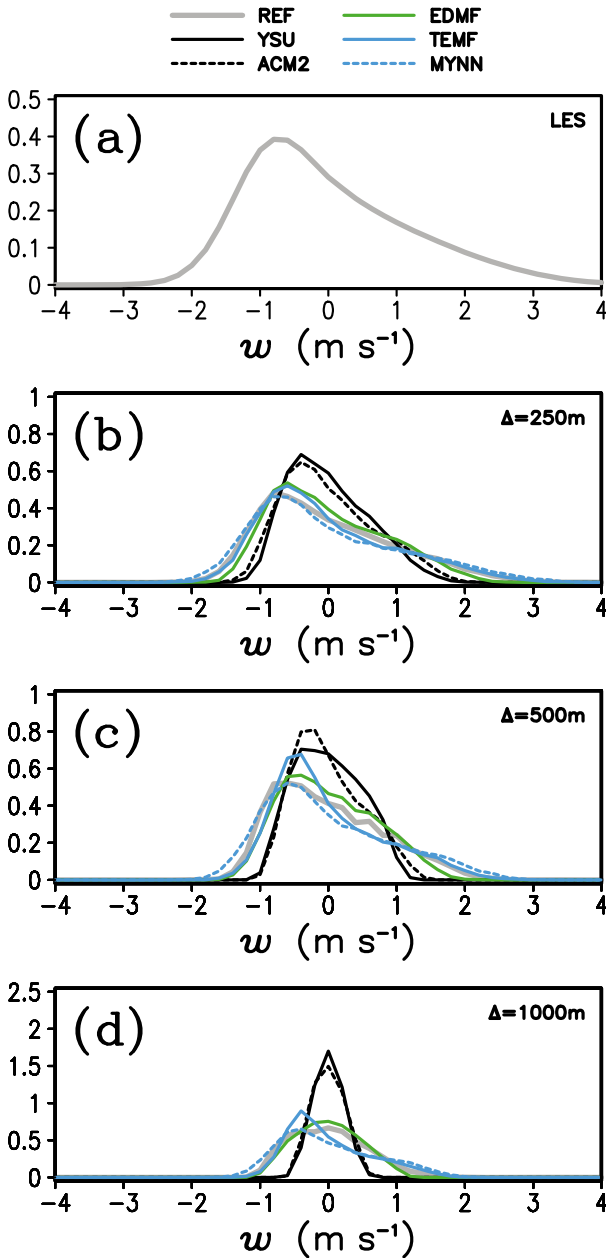


FIG. 9. Probability density functions (PDFs) of vertical velocity ( $w$ ) at  $0.5z_i$  (a) for LES, and for experiments with  $\Delta$  of (b) 250, (c) 500, and (d) 1000 m. PDFs for YSU (solid black), ACM2 (dotted black), EDMF (solid green), TEMF (solid blue), and MYNN (dotted blue) experiments are presented with corresponding reference (solid gray). Results for  $N_z = 100$  are shown.

the energy spectrum and vice versa; for example, for 500-m grid spacing, the PDF for the EDMF experiment is the closest to the reference PDF (cf. Fig. 9c), while the EDMF scheme is not the best scheme in terms of the energy spectrum (cf. Fig. 8b). To find reasons for the discrepancy in the performance of the EDMF

scheme for the different variables, PDFs for filtered  $w$  fields are calculated: the EDMF experiment and reference for 500-m grid spacing.

- 1) First of all,  $w$  fields over the horizontal domain are converted to spectral coefficients over a wave domain using the Fourier transform.
- 2) Then, the inverse Fourier transform is conducted with various cutoff wavelengths ( $\lambda_c$ ) (i.e.,  $2\Delta < \lambda_c < D$ ) to build low-pass filtered  $w$  fields for each  $\lambda_c$ .
- 3) Then, a PDF is calculated for each  $\lambda_c$ .

In Fig. 10, the PDFs for the filtered  $w$  fields with  $\lambda_c$  of 1 km and  $\lambda_c$  of 2 km are presented with the PDFs for the nonfiltered  $w$  fields (i.e.,  $\lambda_c = 0.5$  km). The PDFs with  $\lambda_c$  of 0.5 km are identical to the PDFs in Fig. 9c.

Figure 10a shows the reference PDFs for 500-m grid size at various  $\lambda_c$ :  $\lambda_c = 500$  m, 1 km, and 2 km. The reference PDF for 0.5-km  $\lambda_c$  is positively skewed and there are a number of grid points for strong updrafts and/or downdrafts ( $|w| \geq 1 \text{ m s}^{-1}$ ). On the other hand, the reference PDF for 1-km  $\lambda_c$  is nearly symmetric. The number of grid points for the strong vertical motions for 1-km  $\lambda_c$  is less than half of the number for the nonfiltered PDF. This indicates that the strong vertical motions in the reference mainly have horizontal scales between 0.5 and 1 km. In line with this, the difference between the reference PDFs for 1-km  $\lambda_c$  and 2-km  $\lambda_c$  implies that the moderate updrafts and downdrafts ( $0.5 < |w| < 1 \text{ m s}^{-1}$ ) are from the motions with the scales between 1 and 2 km.

Figure 10b shows that the nonfiltered PDF for the EDMF experiment is similar to the reference PDF, as shown in Fig. 9c. However, the PDF for 1-km  $\lambda_c$  has similar values to the nonfiltered PDF for the strong updrafts or downdrafts ( $|w| \geq 1 \text{ m s}^{-1}$ ). This means that in the EDMF experiment, the motions with scales between 0.5 and 1 km contribute little to the strong vertical motions. On the other hand, the difference between the PDFs for 1-km  $\lambda_c$  and 2-km  $\lambda_c$  is large in the EDMF experiment. This indicates that in the EDMF experiment, the strong vertical velocities are mainly from turbulent motions with scales between 1 and 2 km, while they are from smaller-scale motions (i.e., with scales between 0.5 and 1 km) in the reference.

*e. Flow visualization of resolved vertical velocity*

The visualization of the resolved  $w$  for the horizontal grid size of 500 m is displayed in Fig. 11. As a consequence of the excessive SGS heat transport (Fig. 4) the YSU and ACM2 experiments have suppressed motions with much weaker  $w_{\max}$  and  $w_{\min}$  (Figs. 11b,c). On the other hand, both updrafts and downdrafts appear to be too strong in the MYNN experiment (Fig. 11f), according to the lack of dissipation (Figs. 4 and 8). Values

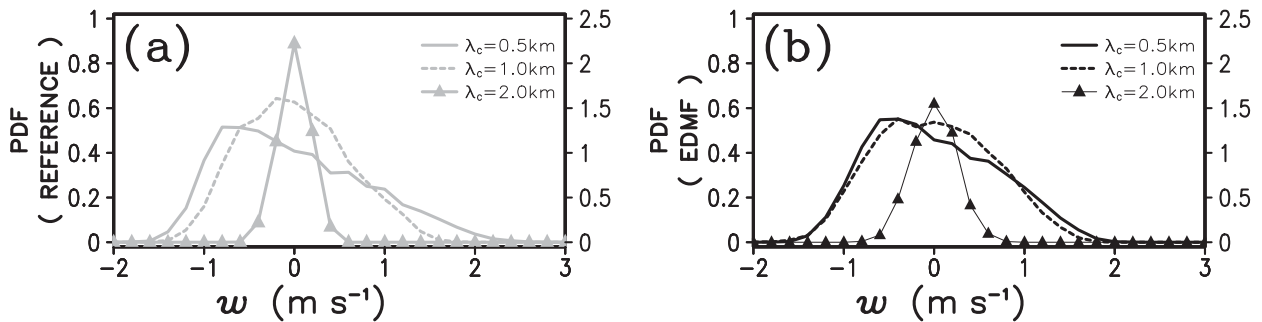


FIG. 10. PDFs of filtered vertical velocity ( $w$ ) fields at  $0.5z_i$  for various cutoff wavelengths ( $\lambda_c$ ): (a) the reference (gray) and (b) the EDMF experiment (black) with 500-m grid spacing. The PDFs are presented for  $\lambda_c$  of 0.5 (solid), 1.0 (dotted), and 2.0 km (solid lines with closed triangles). Note that the PDFs for  $\lambda_c$  of 0.5 km (solid lines) are identical to the PDFs in Fig. 9c. For more details, refer to section 3d.

of  $w_{\max}$  and  $w_{\min}$  calculated by the TEMF experiment (Fig. 11e) are the closest to those in the reference. The  $w$  fields for the EDMF experiment look the most similar to the reference  $w$  in eddy shapes, but the horizontal extent of the updrafts/downdrafts is larger than that for the REF as can be inferred from Fig. 10.

#### 4. Summary and conclusions

This paper evaluated performance of five conventional PBL parameterizations in WRF at subkilometer grid sizes in reproducing turbulence statistics including the PDF of resolved vertical velocity and its scale dependency, energy spectrum, resolved and parameterized vertical fluxes, as well as mean and total vertical flux. The five PBL schemes are the YSU, ACM2, EDMF, TEMF, and MYNN schemes. The reference data for 250-m, 500-m, and 1-km grid sizes were produced by spatially filtering the LES (Shin and Hong 2015) and considered as truth for the grid sizes (e.g., Cheng et al. 2010; Honnert et al. 2011; Dorrestijn et al. 2013; Shin and Hong 2013; Zhou et al. 2014; Honnert et al. 2014; Shin and Hong 2015). Note that this study focused on the parameterization of vertical transport. Horizontal transport is computed by Deardorff's LES SGS parameterization, and the key findings of this study are not sensitive to the parameterization of horizontal transport.

It was confirmed that none of the PBL schemes are scale-aware in the sense of adjusting their resolved and subgrid-scale eddy contributions consistently with the filtered reference data. Instead, each PBL scheme has a rather fixed ratio of subgrid-scale transport to total transport resulting in its own best-performing resolution in parameterizing the SGS transport, which affects the prediction of the resolved energy spectrum. The best grid spacing appears to be different between heat transport and momentum transport. For example, the TEMF

experiment computes the largest SGS momentum transport (possibly related to its highest surface drag), while it calculates the smallest SGS heat transport. Even though the five schemes parameterize different amounts of the transport, they all reproduce total (resolved plus SGS) heat transport well. This is because the resolved heat transport compensates differences between the parameterized heat transport and the reference SGS transport. This interaction between the resolved transport and SGS transport was not found in momentum transport. For other resolved turbulence statistics, it was shown that the schemes that permitted resolved eddies were generally able to capture skewness properties, while the best schemes in reproducing the energy spectrum and PDF of  $w$  do not coincide.

The evaluation results indicate that there is at least one satisfactory parameterization for each of the gray-zone grid sizes and the statistical variables that are tested in this study, even though all the traditional PBL parameterizations have been originally designed only for larger grid spacings. By selecting the best scheme for the user's grid size and purpose, errors owing to the turbulence parameterization can be reduced. However, it should not be a long-term solution. None of the traditional turbulence parameterizations satisfactorily works across all the tested subkilometer grid meshes, for all the tested variables. Our results support the conclusion that more universal parameterizations, which are scale-aware and work for all prognostic variables, are needed.

*Acknowledgments.* We gratefully acknowledge Peggy LeMone at NCAR whose thorough review greatly improved the manuscript, and three anonymous reviewers for providing careful and valuable comments and giving us advice on model sensitivity tests. We would like to acknowledge high-performance computing support from Yellowstone (ark:/85065/d7wd3xhc) provided

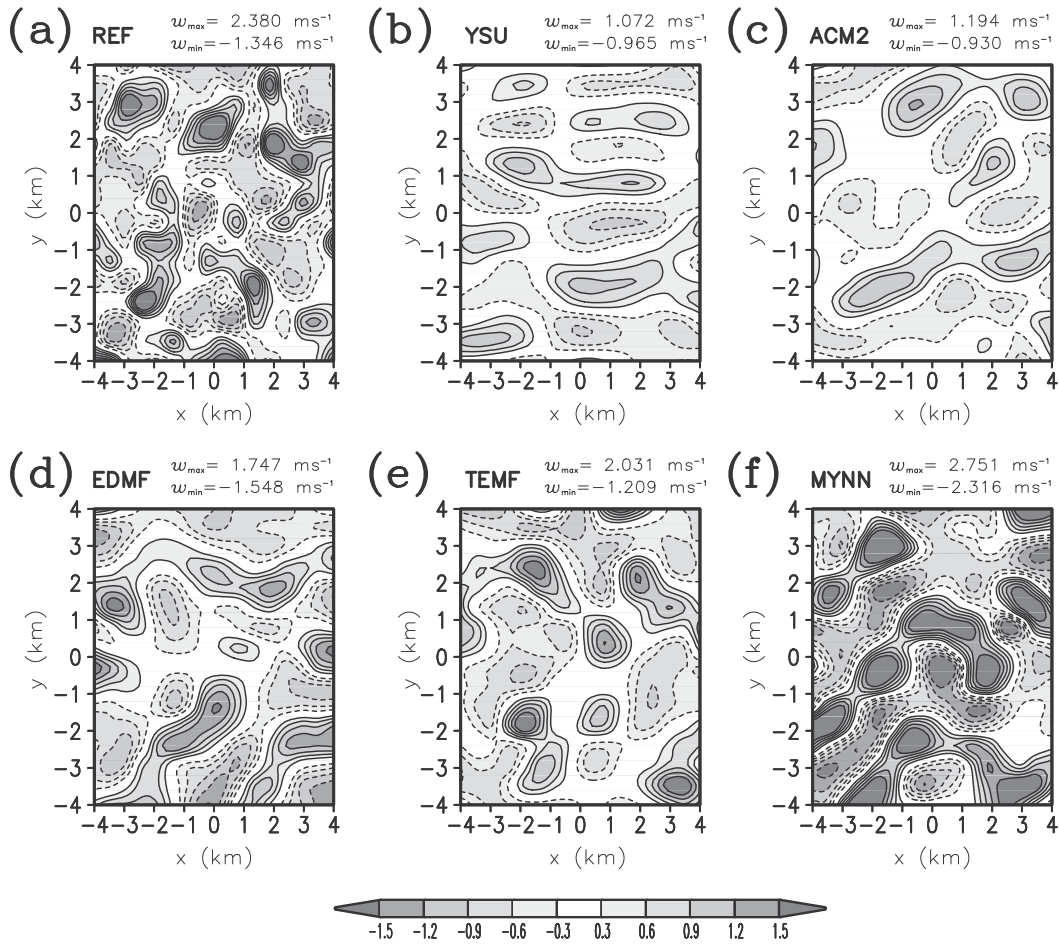


FIG. 11. Instantaneous vertical velocity fields (shaded:  $\text{m s}^{-1}$ ) for  $\Delta$  of 500 m at  $0.5z_i$  at  $3t_0$ , for the (a) REF (b) YSU, (c) ACM2, (d) EDMF, (e) TEMF, and (f) MYNN experiments, with  $w_{\max}$  and  $w_{\min}$  written on the top of each panel. Contours are every  $0.3 \text{ m s}^{-1}$  from  $-1.5$  to  $+1.5 \text{ m s}^{-1}$ . Results for  $N_z = 100$  are shown.

by NCAR’s Computational and Information Systems Laboratory (CISL), sponsored by the National Science Foundation (NSF). The first author also thanks the Advanced Study Program (ASP) at NCAR for post-doctoral support.

APPENDIX

Parameterization of Horizontal Transport

In the WRF model, subgrid-scale (SGS) horizontal transport is parameterized through an eddy-diffusivity form. In the incompressible flows,

$$\frac{\partial \bar{c}^\Delta}{\partial t} = \dots - \frac{\partial \overline{u'_i c^i}}{\partial x_i}, \tag{A1}$$

$$\overline{u'_i c^i} = -K_{\text{HOR},c} \frac{\partial \bar{c}^\Delta}{\partial x_i}, \quad i = 1, 2, \tag{A2}$$

where  $K_{\text{HOR},c}$  is the horizontal diffusivity for the variable  $c$ .

For calculating the horizontal diffusivity, the WRF model provides four options:

- 1)  $K_{\text{HOR}}$  is determined by user-specified constants.
- 2)  $K_{\text{HOR}}$  is determined using prognostic turbulent kinetic energy (TKE) and model grid size ( $\Delta$ ).
- 3)  $K_{\text{HOR}}$  is determined using three-dimensional deformation and  $\Delta$ .
- 4)  $K_{\text{HOR}}$  is determined using two-dimensional horizontal deformation and  $\Delta$ .

The second option (the 1.5-order TKE closure; Deardorff 1980) is selected in this study, and  $K_{\text{HOR}}$  is calculated as below:

$$K_{\text{HOR}(u,v)} = C_k l_{\text{SGS}} \sqrt{e}, \tag{A3}$$

$$K_{\text{HOR}(\theta,q)} = K_{\text{HOR}(u,v)} \text{Pr}_t^{-1}. \tag{A4}$$

In Eq. (A3),  $C_k$  is a constant (0.1),  $l_{\text{SGS}}$  is a SGS mixing length scale, and  $e$  is the TKE. In Eq. (A4),  $\text{Pr}_t$  is a turbulent Prandtl number:  $\text{Pr}_t^{-1} = 1 + 2l_{\text{SGS}}(\Delta x \Delta y \Delta z)^{1/3}$ .

The SGS length scale is calculated as

$$l_{\text{SGS}} = \begin{cases} \min(\Lambda, 0.76\sqrt{e}/N) & \text{for } N^2 > 0 \\ \Lambda & \text{for } N^2 \leq 0 \end{cases} \quad (\text{A5})$$

$$\Lambda = \sqrt{\Delta x \Delta y \Delta z}, \quad (\text{A6})$$

where  $N$  is the Brunt–Väisälä frequency. More details for other options are documented in section 4.2.3 in Skamarock et al. (2008).

Note that Deardorff's TKE closure has been frequently used for parameterizing SGS horizontal transport in cloud-resolving models (CRMs) at subkilometer and kilometer grid sizes (Bryan et al. 2003). However, there are several issues of using the TKE closure in our experimental setup, requiring comments on them.

First of all, the options 2 and 3 above were originally designed as SGS turbulence closures for LES models, requiring a model filter in the inertial subrange. Using them at subkilometer and kilometer grid sizes, which are above the scale of the inertial subrange, is not appropriate for their design (Bryan et al. 2003). The absence of proper horizontal transport parameterizations for the grid sizes is one aspect of turbulence modeling in the “terra incognita” or “gray zone,” while this study is limited to the vertical transport. Evaluating and developing horizontal transport parameterizations for the gray zone are beyond the scope of this study.

Second, previous CRM studies adopted the LES SGS closures for parameterizing both horizontal and vertical transport, while we use the TKE closure for horizontal transport and PBL parameterizations for vertical transport: a hybrid combination is used. Note that all meso-scale models have some kind of horizontal diffusion, and it is more general to run the models with it than without any: either explicit numerical diffusion (Kniewel et al. 2007; Langhans et al. 2012) and/or physically based horizontal diffusion (Rotunno et al. 2009; Parodi and Tanelli 2010; Zhu et al. 2014; Hanley et al. 2015). However, there are no proper horizontal turbulence parameterizations for the gray zone yet, as mentioned above. Accordingly, to test the robustness of our results we conducted two additional sensitivity sets of experiments using different horizontal diffusion schemes: one with  $K_{\text{HOR}}$  determined using two-dimensional horizontal deformation and  $\Delta$  (i.e., option 4 above) and the other one with  $K_{\text{HOR}} = 0$ . The sensitivity test confirmed that the results for the ideal CBL case in this study are not sensitive to the parameterization of horizontal diffusion.

## REFERENCES

- Angevine, W. M., H. Jiang, and T. Mauritsen, 2010: Performance of an eddy diffusivity-mass flux scheme for shallow cumulus boundary layers. *Mon. Wea. Rev.*, **138**, 2895–2912, doi:10.1175/2010MWR3142.1.
- Boutle, I. A., J. E. J. Eyre, and A. P. Lock, 2014: Seamless strato-cumulus simulation across the turbulent gray zone. *Mon. Wea. Rev.*, **142**, 1655–1668, doi:10.1175/MWR-D-13-00229.1.
- Bretherton, C. S., and S. Park, 2009: A new moist turbulence parameterization in the Community Atmospheric Model. *J. Climate*, **22**, 3422–3448, doi:10.1175/2008JCLI2556.1.
- Bryan, G. H., J. C. Wyngaard, and J. M. Fritsch, 2003: Resolution requirements for the simulation of deep moisture convection. *Mon. Wea. Rev.*, **131**, 2394–2416, doi:10.1175/1520-0493(2003)131<2394:RRFTSO>2.0.CO;2.
- Cheng, A., K.-M. Xu, and B. Stevens, 2010: Effects of resolution on the simulation of boundary-layer clouds and the partition of kinetic energy to subgrid scales. *J. Adv. Model. Earth Syst.*, **2** (3), doi:10.3894/JAMES.2010.2.3.
- Ching, J., R. Rotunno, M. A. LeMone, A. Martilli, B. Kosovic, P. A. Jimenez, and J. Dudhia, 2014: Convectively induced secondary circulations in fine-grid mesoscale numerical weather prediction models. *Mon. Wea. Rev.*, **142**, 3284–3302, doi:10.1175/MWR-D-13-00318.1.
- Deardorff, J. W., 1980: Stratocumulus-capped mixed layers derived from a three-dimensional model. *Bound.-Layer Meteor.*, **18**, 495–527, doi:10.1007/BF00119502.
- Dorrestijn, J., D. T. Crommelin, A. P. Siebesma, and H. J. J. Jonker, 2013: Stochastic parameterization of shallow cumulus convection estimated from high-resolution model data. *Theor. Comput. Fluid Dyn.*, **27**, 133–148, doi:10.1007/s00162-012-0281-y.
- Efstathiou, G. A., and R. J. Beare, 2015: Quantifying and improving sub-grid diffusion in the boundary-layer grey zone. *Quart. J. Roy. Meteor. Soc.*, **141**, 3006–3017, doi:10.1002/qj.2585.
- Hanley, K. E., R. S. Plant, T. H. M. Stein, R. J. Hogan, J. C. Nicol, H. W. Lean, C. Halliwell, and P. A. Clark, 2015: Mixing-length controls on high-resolution simulations of convective storms. *Quart. J. Roy. Meteor. Soc.*, **141**, 272–284, doi:10.1002/qj.2356.
- Holtstlag, A. A. M., and B. A. Boville, 1993: Local versus non-local boundary-layer diffusion in a global climate model. *J. Climate*, **6**, 1825–1842, doi:10.1175/1520-0442(1993)006<1825:LVNBLD>2.0.CO;2.
- Hong, S.-Y., and H.-L. Pan, 1996: Nonlocal boundary layer vertical diffusion in a medium-range forecast model. *Mon. Wea. Rev.*, **124**, 2322–2339, doi:10.1175/1520-0493(1996)124<2322:NBLVDI>2.0.CO;2.
- , Y. Noh, and J. Dudhia, 2006: A new vertical diffusion package with an explicit treatment of entrainment processes. *Mon. Wea. Rev.*, **134**, 2318–2341, doi:10.1175/MWR3199.1.
- Honnert, R., V. Masson, and F. Couvreux, 2011: A diagnostic for evaluating the representation of turbulence in atmospheric models at the kilometric scale. *J. Atmos. Sci.*, **68**, 3112–3131, doi:10.1175/JAS-D-11-061.1.
- , —, and —, 2014: What is new in the gray zone? *21st Symp. on Boundary Layers and Turbulence*, Leeds, United Kingdom, Amer. Meteor. Soc., 17B.2. [Available online at <https://ams.confex.com/ams/21BLT/webprogram/Paper248579.html>.]
- Hu, X.-M., J. W. Nielsen-Gammon, and F. Zhang, 2010: Evaluation of three planetary boundary layer schemes in the WRF



- model. *J. Appl. Meteor. Climatol.*, **49**, 1831–1844, doi:10.1175/2010JAMC2432.1.
- Huang, Q., J. H. Marsham, D. J. Parker, W. Tian, and T. Weckwerth, 2009: A comparison of roll and nonroll convection and the subsequent deepening moist convection: An LEM case study base on SCMS data. *Mon. Wea. Rev.*, **137**, 350–365, doi:10.1175/2008MWR2450.1.
- Ito, J., H. Niino, M. Nakanishi, and C. H. Moeng, 2015: An extension of the Mellor-Yamada model to the terra incognita zone for dry convective mixed layers in the free convection regime. *Bound.-Layer Meteorol.*, **157**, 23–43, doi:10.1007/s10546-015-0045-5.
- Janjic, Z., 1994: The step-mountain Eta coordinate model: Future developments of the convection, viscous sublayer, and turbulence closure schemes. *Mon. Wea. Rev.*, **122**, 927–945, doi:10.1175/1520-0493(1994)122<0927:TSMECM>2.0.CO;2.
- Kniewel, J. C., G. H. Bryan, and J. P. Hacker, 2007: Explicit numerical diffusion in the WRF model. *Mon. Wea. Rev.*, **135**, 3808–3824, doi:10.1175/2007MWR2100.1.
- Langhans, W., J. Schmidli, and C. Schär, 2012: Mesoscale impacts of explicit numerical diffusion in a convection-permitting model. *Mon. Wea. Rev.*, **140**, 226–244, doi:10.1175/2011MWR3650.1.
- LeMone, M. A., M. Tewari, F. Chen, and J. Dudhia, 2013: Objectively determined fair-weather CBL depths in the ARW-WRF model and their comparison to CASES-97 observations. *Mon. Wea. Rev.*, **141**, 30–54, doi:10.1175/MWR-D-12-00106.1.
- Li, X., and Z. Pu, 2008: Sensitivity of numerical simulation of early rapid intensification of Hurricane Emily (2005) to cloud microphysics and planetary boundary layer parameterizations. *Mon. Wea. Rev.*, **136**, 4819–4838, doi:10.1175/2008MWR2366.1.
- Mellor, G. L., and T. Yamada, 1982: Development of a turbulence closure model for geophysical fluid problems. *Rev. Geophys. Space Phys.*, **20**, 851–875, doi:10.1029/RG020i004p00851.
- Moeng, C.-H., and P. P. Sullivan, 1994: A comparison of shear- and buoyancy-driven planetary boundary layer flows. *J. Atmos. Sci.*, **51**, 999–1022, doi:10.1175/1520-0469(1994)051<0999:ACOSAB>2.0.CO;2.
- Nakanishi, M., and H. Niino, 2009: Development of an improved turbulence closure model for the atmospheric boundary layer. *J. Meteor. Soc. Japan*, **87**, 895–912, doi:10.2151/jmsj.87.895.
- Parodi, A., and S. Tanelli, 2010: Influence of turbulence parameterizations on high-resolution numerical modeling of tropical convection observed during the TC4 field campaign. *J. Geophys. Res.*, **115**, D00J14, doi:10.1029/2009JD013302.
- Pergaud, J., V. Masson, S. Malardel, and F. Couvreux, 2009: A parameterization of dry thermals and shallow cumuli for mesoscale numerical weather prediction. *Bound.-Layer Meteorol.*, **132**, 83–106, doi:10.1007/s10546-009-9388-0.
- Pleim, J. E., 2007a: A combined local and nonlocal closure model for the atmospheric boundary layer. Part I: Model description and testing. *J. Appl. Meteor. Climatol.*, **46**, 1383–1395, doi:10.1175/JAM2539.1.
- , 2007b: A combined local and nonlocal closure model for the atmospheric boundary layer. Part II: Application and evaluation in a mesoscale meteorological model. *J. Appl. Meteor. Climatol.*, **46**, 1396–1409, doi:10.1175/JAM2534.1.
- Rotunno, R., Y. Chen, W. Wang, C. Davis, J. Dudhia, and G. J. Holland, 2009: Large-eddy simulation of an idealized tropical cyclone. *Bull. Amer. Meteor. Soc.*, **90**, 1783–1788, doi:10.1175/2009BAMS2884.1.
- Shin, H. H., and S.-Y. Hong, 2011: Intercomparison of planetary boundary-layer parametrizations in the WRF model for a single day from CASES-99. *Bound.-Layer Meteorol.*, **139**, 261–281, doi:10.1007/s10546-010-9583-z.
- , and —, 2013: Analysis on resolved and parameterized vertical transports in the convective boundary layers at the gray-zone resolutions. *J. Atmos. Sci.*, **70**, 3248–3261, doi:10.1175/JAS-D-12-0290.1.
- , and —, 2015: Representation of the subgrid-scale turbulent transport in convective boundary layers at gray-zone resolutions. *Mon. Wea. Rev.*, **143**, 250–271, doi:10.1175/MWR-D-14-00116.1.
- , —, and J. Dudhia, 2012: Impacts of the lowest model level height on the performance of planetary boundary layer parameterizations. *Mon. Wea. Rev.*, **140**, 664–682, doi:10.1175/MWR-D-11-00027.1.
- Skamarock, W. C., 2004: Evaluating mesoscale NWP models using kinetic energy spectra. *Mon. Wea. Rev.*, **132**, 3019–3032, doi:10.1175/MWR2830.1.
- , and Coauthors, 2008: A description of the Advanced Research WRF version 3. NCAR Tech. Note NCAR/TN-475+STR, 113 pp., doi:10.5065/D68S4MVH.
- Steenefeld, G. J., T. Mauritsen, E. I. F. de Bruijn, J. V.-G. de Arellano, G. Svensson, and A. A. M. Holtslag, 2008: Evaluation of limited-area models for the representation of the diurnal cycle and contrasting nights in CASES-99. *J. Appl. Meteor. Climatol.*, **47**, 869–887, doi:10.1175/2007JAMC1702.1.
- Stull, R. B., 1988: *An Introduction to Boundary Layer Meteorology*. Kluwer Academic, 666 pp.
- Sullivan, P. P., and E. G. Patton, 2011: The effect of mesh resolution on convective boundary layer statistics and structures generated by large-eddy simulation. *J. Atmos. Sci.*, **68**, 2395–2415, doi:10.1175/JAS-D-10-05010.1.
- Sykes, R. I., and D. S. Henn, 1989: Large-eddy simulation of turbulent sheared convection. *J. Atmos. Sci.*, **46**, 1106–1118, doi:10.1175/1520-0469(1989)046<1106:LESOTS>2.0.CO;2.
- Troen, I. B., and L. Mahrt, 1986: A simple model of the atmospheric boundary layer; sensitivity to surface evaporation. *Bound.-Layer Meteorol.*, **37**, 129–148, doi:10.1007/BF00122760.
- Wyngaard, J. C., 2004: Toward numerical modeling in the “terra incognita.” *J. Atmos. Sci.*, **61**, 1816–1826, doi:10.1175/1520-0469(2004)061<1816:TNMITT>2.0.CO;2.
- , 2010: *Turbulence in the Atmosphere*. Cambridge University Press, 393 pp.
- Zhou, B., J. S. Simon, and F. K. Chow, 2014: The convective boundary layer in the terra incognita. *J. Atmos. Sci.*, **71**, 2545–2563, doi:10.1175/JAS-D-13-0356.1.
- Zhu, P., K. Menelaou, and Z. Zhu, 2014: Impact of subgrid-scale vertical turbulent mixing on eyewall asymmetric structures and mesovortices of hurricanes. *Quart. J. Roy. Meteor. Soc.*, **140**, 416–438, doi:10.1002/qj.2147.